Letter

Enhanced Terahertz Detection Efficiency via Grating-Assisted Noncollinear Electro-Optic Sampling

Alexei Halpin,[1,*] Wei Cui,[1] Aidan W. Schiff-Kearn,[1] Kashif Masud Awan,[2] Ksenia Dolgaleva,[1,3] and Jean-Michel Ménard[1,†]

[1] *Department of Physics, University of Ottawa, 25 Templeton Street, Ottawa, Ontario K1N 6N5, Canada*
[2] *Stewart Blusson, Quantum Matter Institute, 2355 East Mall, Vancouver, British Columbia V6T 1Z4, Canada*
[3] *School of Electrical Engineering and Computer Science, University of Ottawa, 25 Templeton Street, Ottawa, Ontario K1N 6N5, Canada*

(Received 13 March 2019; revised manuscript received 17 June 2019; published 26 September 2019; corrected 18 August 2020)

Sensitive detection of phase-locked terahertz (THz) pulses is routinely achieved using electro-optic sampling (EOS), a technique that harnesses second-order optical nonlinearities in a crystalline semiconductor. The thickness and electro-optic coefficient of such a crystal set the detection sensitivity in EOS, while its linear optical properties often determine the accessible detection bandwidth through the phase-matching conditions. Here, we demonstrate how a periodically patterned structure on the incident surface of an EOS crystal can be used to overcome bandwidth limitations by enabling noncollinear propagation between the THz waves and a near-infrared (NIR) gating pulse. The concept is demonstrated with phase gratings etched on a 1-mm-thick gallium phosphide (GaP) semiconductor. The use of a diffracted NIR gating pulse to retrieve the THz waveform results in a sensitivity enhancement of a factor of approximately 2 with regard to the spectral maximum at 2 THz and exceeding an order of magnitude at 5 THz. This extends the spectral detection bandwidth up to 5 THz, which is twice as large as that achievable in a similar configuration with collinear THz and NIR pulses, facilitating the broadband detection of weak signals in THz spectroscopy.

DOI: 10.1103/PhysRevApplied.12.031003

Terahertz (THz) science is a fast-growing field with contributions to the fundamental research into emerging optoelectronic materials [1–3] and the development of novel forms of ultrafast microscopy [4–7], as well as applications in next-generation telecommunications [8]. In this respect, there is continued progress and research toward the efficient generation, detection, and routing of THz radiation. Nonlinear crystals remain the workhorse emitters and receivers for researchers, particularly in the fields of spectroscopy and high-field generation. Typically, the second-order nonlinearity of these crystals is exploited for generation via optical rectification and for detection through electro-optic sampling (EOS) [9,10]. In the standard EOS configuration, a local THz field rotates the polarization of a copropagating near-infrared (NIR) femtosecond pulse via the Pockels effect. The THz field can then be reconstructed by monitoring the induced change in polarization of the NIR beam while it is scanned in the time domain across the oscillating THz transient.

The sensitivity and detection bandwidth afforded by EOS lends great versatility to the technique, resulting in the widespread application of EOS in THz spectroscopy. On the one hand, the sensitivity of EOS allows us to probe very weak nonlinear signals [11] or even fluctuations of the quantum vacuum [12,13]. On the other hand, the contact-free measurement of the (photo)conductivity of materials benefits from the broad detection bandwidth provided by EOS, by allowing a more accurate determination of the complex conductivity of the sample in question. EOS detection crystals with extremely high second-order nonlinear coefficients could greatly facilitate experiments that demand high sensitivity due to weak signal fields, while decreasing acquisition times. However, a material that possesses such a strong nonlinearity as well as linear properties providing a flat detection response over a large THz bandwidth is still missing.

The use of thick crystals can improve sensitivity, by increasing the nonlinear interaction length between the NIR gating pulse and the THz wave. Maximization of the bandwidth can also be achieved by using very short gating pulses or by employing spectrally resolved EOS [14]; however, these approaches are also limited in bandwidth by material properties. Specifically, the linear optical

*alexeihalpin@gmail.com
†jean-michel.menard@uottawa.ca

properties of the crystals define the associated phase-matching conditions for EOS for a given crystal thickness, setting the effective spectral range for the generation [15] and detection [16] of THz pulses. For birefringent materials, the optimization of the phase-matching bandwidth through angle tuning has previously been applied to EOS over a vast range of frequencies in the THz spectrum [17], but this recourse is not available for all crystals. As a result, experimentalists usually opt for the crystal that offers the best compromise between sensitivity and spectral bandwidth based on the nature of the experiment.

Here, we propose to overcome the detection phase-matching restrictions that limit the use of thicker nonlinear crystals by exploiting a noncollinear phase-matching geometry, enabled by a periodic index modulation defined at the surface of the crystal and acting as a phase grating. The use of a freestanding grating to tilt the pulse front of NIR pulses has already been demonstrated to improve conversion efficiency in the THz generation process. This improvement can be understood through better phase matching of the NIR pulses and the generated THz fields through a noncollinear geometry, resulting in a longer coherence length. This geometry has been adopted as the standard method for high-field THz generation in $LiNbO_3$ [18,19] and has successfully been applied to other materials [20]. Also in the context of THz generation, the use of a surface grating on a semiconductor has previously been considered as an alternative to an external grating. Theoretical work has shown that this approach can be used for high-field THz generation in ZnTe [21,22] and the concept has been demonstrated experimentally with $LiNbO_3$ [23,24].

We consider a phase grating at the surface of a nonlinear semiconductor to achieve enhanced THz detection by EOS. The surface grating can be used to arbitrarily tilt the wave vector of the NIR gating pulse inside the crystal, thereby customizing the phase-matching conditions. Our grating-assisted noncollinear geometry relies on a standard EOS configuration, with both NIR and THz pulses normally incident on the EOS crystal. The only modification to the standard alignment is the collection of a diffracted beam following the detection crystal for polarization analysis. Moreover, the possibility of patterning many phase gratings on the surface of a single EOS crystal can be useful to vary the phase-matching conditions and tune the detection spectral window. For these reasons, we believe our scheme to be more flexible and easier to implement than a fully noncollinear detection scheme [25].

In our experiments, we use a ⟨110⟩-oriented gallium phosphide (GaP) semiconductor as an EOS crystal [26]. Our method could be easily generalized to other materials. Although the periodic surface modulations considered in our experiment are optimized for the detection of three frequencies at 3, 4, and 5 THz, our results show a broadening of the detection spectral window without loss of sensitivity at the low-frequency range. These results are supported by numerical simulations. In addition, we demonstrate that the overall signal-detection efficiency is increased through another mechanism, which is the removal of the common-mode signal in the EOS as a consequence of favorable Fresnel reflections at the back surface of the crystal. In brief, our approach increases both the bandwidth and sensitivity of nonlinear crystal-based EOS while maintaining a simple collinear alignment of the incident NIR gating and the THz pulses.

The experiments are carried out using a conventional THz time-domain spectroscopy instrument, as shown in Fig. 1(a). The laser system used for these studies is a Yb:KGW regenerative amplifier producing laser pulses at $\lambda = 1.035$ μm with an 180-fs pulse duration. The pulses are launched into an Ar-filled hollow-core kagomé photonic crystal fiber (HC PCF), in which self-phase modulation broadens the NIR spectrum. The pulses are recompressed using chirped mirrors to a duration of 50 fs, approaching the transform limit for a 10-THz bandwidth. Similar configurations have recently been demonstrated to achieve broadband THz generation and detection [26,27].

In the THz spectrometer, the NIR pulses are split along two arms. In the first arm, THz pulses are generated by optical rectification inside a ⟨110⟩-oriented 0.2-mm-thick GaP crystal. In the second arm, gating pulses are delayed relative to the THz pulse with a linear-translation stage. Both the THz and the gating pulses are initially collinear before they are focused by an off-axis parabolic mirror onto the detection crystal. The transmitted gating beam is then collimated with a lens and analyzed using polarization optics and a balanced photodiode pair.

In most implementations, the thickness of the detection crystal is chosen on the basis of the bandwidth of interest. Thicker crystals usually lead to larger signal amplitudes in EOS due to a longer nonlinear interaction length with the THz pulse, but the detection spectral range is then reduced and often structured as a result of phase mismatch. Conversely, for a thinner detection crystal, the phase-matching conditions are less stringent and the spectral response is therefore broader. This broadening, however, comes at the expense of detection efficiency, which is reduced due to a shorter nonlinear interaction length.

In Fig. 1(b), we experimentally demonstrate the restriction set by the phase-matching conditions in conventional crystals with different thicknesses: the thicker crystal (1 mm) exhibits a larger detected signal amplitude; however, the maximum sensitivity shifts toward lower frequencies. The thinner crystal (100 μm) provides a flat response over a large spectral range, with a somewhat higher efficiency at higher frequencies compared to that observed in thicker crystals. The 300-μm-thick crystal corresponds to an intermediate case. All measured spectra are normalized by a reference value corresponding to the

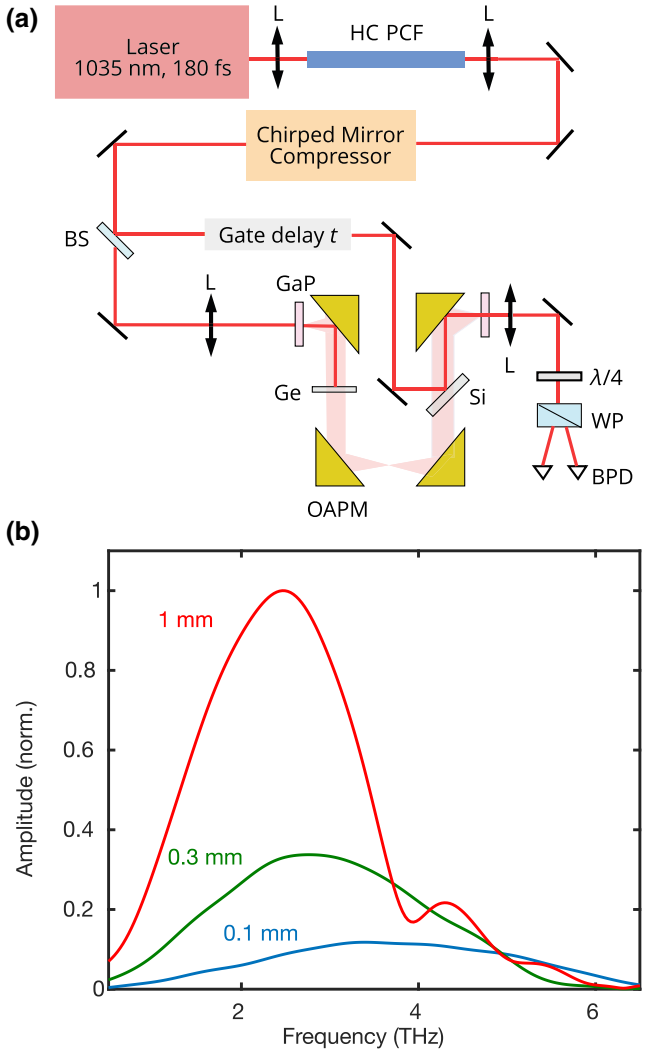

FIG. 1. (a) The experimental layout. The abbreviations are as follows: L, lens; HC PCF, hollow-core photonic crystal fiber; BS, beam splitter; OAPM, off-axis parabolic mirror; Ge, germanium wafer; Si, silicon wafer; λ/4, quarter-wave plate; WP, Wollaston prism; BPD, balanced photodiode pair. The chirped mirror compressor consists of a pair of dielectric mirrors used to compensate for group-velocity dispersion and to compress the NIR pulses. (b) The measured THz spectra for different values of the detector-crystal thickness (red, 1 mm; green, 0.3 mm; blue, 0.1 mm). A 0.2-mm-thick GaP crystal is used for THz generation.

maximum amplitude detected with the 1-mm-thick GaP detection crystal.

The general schematic of our noncollinear detection is illustrated in Fig. 2. The wave-vector diagram corresponding to the detection process can be understood through a combination of sum-frequency-generation (SFG) and difference-frequency-generation (DFG) effects [10] between the NIR gating beam and the THz field. The group velocity of the NIR pulses is greater than the phase velocity of the THz waves for the frequencies considered here in GaP. By introducing a phase grating, the gating

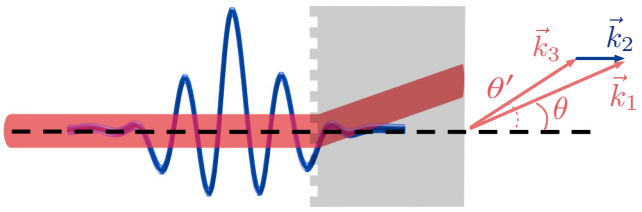

FIG. 2. The modification of gating-beam propagation due to diffraction into the first order of a grating. The phase-matching condition corresponding to the difference-frequency generation detected using EOS is illustrated using a wave-vector diagram, where $\vec{k}_1$ is the NIR gating-pulse wave vector, $\vec{k}_2$ is the THz wave vector, and $\vec{k}_3$ is the DFG-signal wave vector.

beam is deflected by an angle θ, as shown in Fig. 2, and acquires a pulse-front tilt. Different grating periods allow us to control the phase-matching conditions in this manner, without modifying the general alignment of the setup or introducing external angles between the beams before they interact in the detection crystal.

Gratings are fabricated directly on the surface of a GaP sample using a standard lithographic technique. A diagram of the sample fabrication procedure is shown in Fig. 3(a). First, a positive-tone electron-beam resist ZEP520A is spun at 2500 rpm for 80 s and then baked at 180 °C for 3 min. The grating pattern is written by a 30-kV electron-beam-lithography system (Raith), using a dose of 80 μC/cm^2. The sample is then developed for 7.5 min in N-amyl acetate. The grating is transferred into the semiconductor by plasma etching using a Samco inductively coupled plasma reactive-ion-etching (ICP-RIE) system. We use BCl_3 at 2.5 sccm as the process gas, with a 50-W ICP power and a 25-W radio frequency power at a pressure of 0.15 Pa. An etching time of 2 min and 20 s results in an etch depth of approximately 250 nm. The remaining resist is then stripped using commercially available 1165 remover at 80 °C. In such a way, a phase-grating pattern is transferred onto the GaP surface. Several gratings with dimensions of 500 × 500 μm^2 are fabricated on the same GaP sample. Figure 3(b) shows an electron micrograph of the modulation profile of a typical grating used in our experiments.

Our design is based on a rectangular phase grating, where the phase modulation approaches π to suppress the zeroth transmission order, hence optimizing the diffraction efficiency into the first order. We select a rectangular grating geometry (over a sinusoidal or blazed geometry) since it can be fabricated using standard nanofabrication procedures and it yields a high diffraction efficiency. We measure an efficiency of approximately 20% into each of the first-order beams, approaching the theoretical limit when Fresnel reflections are considered [28]. In our setup, the upper first-order beam is collimated by a lens before being routed to the EOS stage for polarization characterization. The collection of the diffracted beam also conveniently

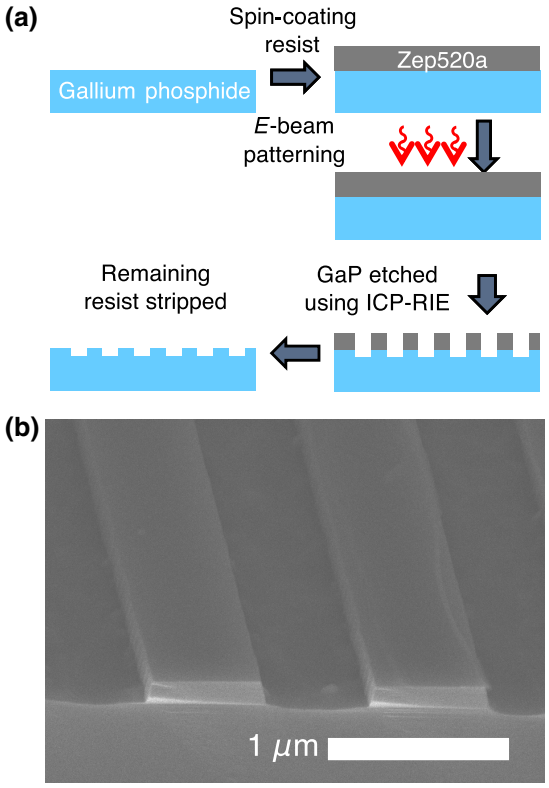

FIG. 3. (a) The fabrication process of phase gratings. (b) A scanning-electron-microscope image of a fabricated grating with a pitch $\Lambda = 1.635\ \mu$m.

reduces "etaloning" of the gating beam in the detection crystal, hence simplifying the subsequent analysis [29].

The precise effect of the grating period on the phase-matching efficiency can be directly calculated from the optical properties of GaP at both NIR [30] and THz [31,32] frequencies. By changing the period or pitch (Λ) of the grating, it is thus possible to define the region of the THz spectrum in which phase mismatch Δk is minimized. We calculate the spectrum detected using electro-optic sampling, for the DFG phase-matching condition:

$$\Delta k = \vec{k}_1(\omega_{\mathrm{NIR}}) - \vec{k}_3(\omega_{\mathrm{NIR}} - \omega_{\mathrm{THz}}) - \vec{k}_2(\omega_{\mathrm{THz}}) \qquad (1)$$

If we consider the diffraction angle of the gating pulse to be θ, we can rewrite the phase-matching condition to account for the noncollinearity introduced by the grating in the crystal, as depicted in Fig. 2:

$$\Delta k_g = k_1(\omega_{\mathrm{NIR}})\cos\theta - k_3(\omega_{\mathrm{NIR}} - \omega_{\mathrm{THz}})\cos\theta' - k_2(\omega_{\mathrm{THz}}) \qquad (2)$$

Here, Δk_g represents the phase mismatch for the patterned samples and θ' is the angle of the DFG signal wave relative to the optical axis, as dictated by the wave vector of the diffracted gating beam. We show the calculated effect of the grating on the phase mismatch in Fig. 4. In panel (a),

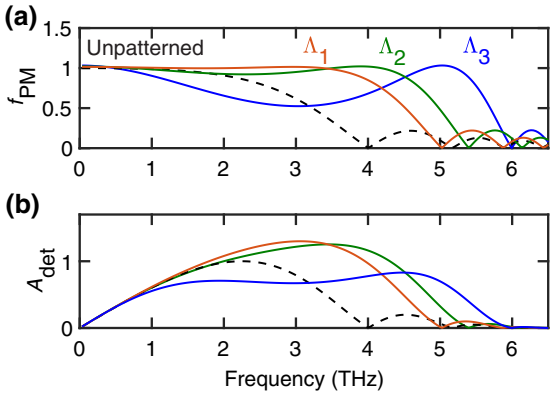

FIG. 4. (a) The phase-matching factor calculated for an unpatterned GaP crystal (black, dashed) and three patterned samples possessing $\Lambda_1 = 1.935\ \mu$m (red), $\Lambda_2 = 1.635\ \mu$m (green), and $\Lambda_3 = 1.335\ \mu$m (blue). All values are computed using material properties taken from Refs. [30–32]. (b) Calculation of the detected THz spectra based on the phase-matching curves, modeled in panel (a), and a 10 THz gating-pulse bandwidth. The values in (a) and (b) for patterned samples are normalized to the maximum values calculated for the unpatterned crystal.

we plot the absolute value for the phase-matching factor f_{PM} in a 1-mm-thick GaP crystal, given by

$$f_{\mathrm{PM}} = \frac{\exp(i\Delta kL - 1)}{i\Delta k}, \qquad (3)$$

for patterned and unpatterned samples, where Δk is the phase mismatch as described in Eqs. (1) and (2) and L is the length of the crystal. We consider three gratings, designed for optimized detection at 3 THz ($\Lambda_1 = 1.935\ \mu$m), 4 THz ($\Lambda_2 = 1.635\ \mu$m), and 5 THz ($\Lambda_3 = 1.335\ \mu$m), respectively. These pitch values are chosen for their corresponding diffraction angle θ minimizing Δk_g in Eq. (2).

Numerical calculations clearly show that grating-assisted noncollinear EOS can allow phase-matching conditions to be satisfied at higher THz frequencies. As the pitch is reduced, the THz detection efficiency moves toward higher frequencies due to the enhancement of f_{PM}. More importantly, this enhancement comes at no cost: there is no reduction in detection efficiency at the lowest end of the THz window.

The values of f_{PM} are independent of the NIR input bandwidth, which plays a role in truncating the detected THz spectrum at both high and low frequencies. In Fig. 4(b), we use the autocorrelation function of the employed NIR pulses to calculate the detected THz spectral amplitude [10]. By accounting for the finite bandwidth of the gating pulse, as well as the spectral dependence of the electro-optic coefficient of GaP [32], we determine that the detected spectral amplitude A_{det} for an unpatterned crystal should peak at roughly 2.2 THz, with a significant drop at approximately 3 THz. Meanwhile, the

detected spectra using the patterned GaP crystals should peak at approximately 3 THz, 3.5 THz, and 4.6 THz, respectively. While our laser bandwidth is approximately 10 THz, for GaP the enhancement of detection toward yet higher frequencies than 5 THz becomes impeded by several factors. First, the electro-optic coefficient vanishes at approximately 7.5 THz [33]. While it becomes appreciable once more at higher frequencies, the strong absorption due to phonons around 11 THz poses a challenge for phase matching [31]. Finally, at higher frequencies, the phase velocity of THz waves is larger than the group velocity of the NIR pulses, such that the grating becomes unhelpful in achieving phase-matching conditions.

Following these calculations, we fabricate the gratings described above and measure the detected THz spectra as a function of the pitch of the grating. Figure 5 shows the three corresponding sets of measured THz spectra for Λ_1 (red), Λ_2 (green), and Λ_3 (blue). The black dashed line is a reference trace taken using an unpatterned region on the same GaP crystal. For all traces, the signals are first normalized to the fluence of the NIR pulse incident on the balanced photodiode pair during EOS and then divided by the maximum amplitude of the reference signal. The results obtained with the grating-assisted EOS show a significant enhancement of the detection efficiency at THz frequencies above 2.5 THz. With shorter grating periods, we also observe that the spectral detection window consistently extends toward higher frequencies, in agreement with the phase-matching calculations. Furthermore, we gain one order of magnitude in detection sensitivity at 5 THz. The bandwidth of the detected THz spectra now extends over 5 THz, twice that of the reference spectra, in good agreement with the model in Fig. 4.

By comparing the reference to other results in Fig. 5, we note that grating-assisted EOS also provides an overall increase in detection efficiency. This is due to a filtering effect that separates the signal from the background, as has been previously demonstrated [34,35]. In our scheme, the incident gating beam is *s*-polarized. Following interaction with the THz field, a *p*-polarized frequency-shifted replica of the gating pulse is generated. At the back surface of the crystal, *s*-polarized NIR photons that do not participate in DFG are preferentially reflected, thus reducing the background such that the NIR light reaching our BPD contains proportionally more signal.

In summary, we demonstrate a grating-assisted EOS method relying on a periodically structured nonlinear crystal to customize the phase-matching conditions. Using this method, we achieve a detection spectral window reaching 5 THz, for a crystal possessing a thickness that would otherwise prohibit efficient detection above 3 THz. This enhancement in detection bandwidth does not occur at the expense of sensitivity to low frequencies. On the contrary, we observe an overall increase in the detection efficiency, which further motivates the use of contact gratings for spectroscopy. The gratings can be fabricated by a series of nanofabrication techniques and the general scheme is easy to introduce into conventional THz instruments. While the material GaP restricts further enhancements toward broader bandwidths, the fabrication can be adapted to other crystals, potentially widening the range of electro-optic materials for broadband THz spectroscopy. Finally, since the fabrication is scalable, it is straightforward to extend the proof-of-concept results shown here to more complex patterns, such as chirped gratings for easily tunable detection sources. This method shows great promise to increase the detection efficiency in low-power experiments, such as those involving oscillator sources. We expect this approach to become broadly used for sensitive and broadband applications in ultrafast terahertz photonics.

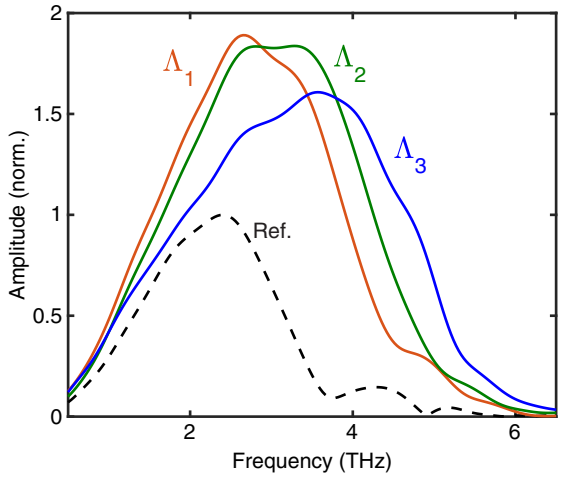

FIG. 5. Experimentally measured THz spectra for a 1-mm-thick GaP crystal, for grating pitches $\Lambda_1 = 1.935$ μm (red), $\Lambda_2 = 1.635$ μm (green), and $\Lambda_3 = 1.335$ μm (blue), as well as on an unpatterned reference (black, dashed). The detection efficiency increases for all patterned samples, while the detection spectrum shifts to higher frequencies as the pitch is decreased.

Acknowledgments This research was supported by the National Sciences and Engineering Research Council (NSERC), Canada Foundation for Innovation (CFI), the Government of Ontario, the Ministry of Research and Innovation (MRI) Ontario Research Fund, and OZ Optics.

[1] C. J. Docherty, P. Parkinson, H. J. Joyce, M. H. Chiu, C. H. Chen, M. Y. Lee, L. J. Li, L. M. Herz, and M. B. Johnston, Ultrafast transient terahertz conductivity of monolayer MoS_2 and WSe_2 grown by chemical vapor deposition, ACS Nano **8**, 11147 (2014).

[2] D. A. Valverde-Chávez, C. S. Ponseca, C. C. Stoumpos, A. Yartsev, M. G. Kanatzidis, V. Sundström, and D. G. Cooke, Intrinsic femtosecond charge generation dynamics in single crystal $CH_3NH_3PbI_3$, Energy Environ. Sci. **8**, 3700 (2015).

[3] F. Langer, C. P. Schmid, S. Schlauderer, M. Gmitra, J. Fabian, P. Nagler, C. Schüller, T. Korn, P. G. Hawkins,

J. T. Steiner, U. Huttner, S. W. Koch, M. Kira, and R. Huber, Lightwave valleytronics in a monolayer of tungsten diselenide, Nature **557**, 76 (2018).

[4] T. L. Cocker, V. Jelic, M. Gupta, S. J. Molesky, J. A. J. Burgess, G. De Los Reyes, L. V. Titova, Y. Y. Tsui, M. R. Freeman, and F. A. Hegmann, An ultrafast terahertz scanning tunnelling microscope, Nat. Photonics **7**, 620 (2013).

[5] M. Eisele, T. L. Cocker, M. A. Huber, M. Plankl, L. Viti, D. Ercolani, L. Sorba, M. S. Vitiello, and R. Huber, Ultrafast multi-terahertz nano-spectroscopy with sub-cycle temporal resolution, Nat. Photonics **8**, 841 (2014).

[6] P. Alonso-González, A. Y. Nikitin, Y. Gao, A. Woessner, M. B. Lundeberg, A. Principi, N. Forcellini, W. Yan, S. Vélez, A. J. Huber, K. Watanabe, T. Taniguchi, F. Casanova, L. E. Hueso, M. Polini, J. Hone, F. H. L. Koppens, and R. Hillenbrand, Acoustic terahertz graphene plasmons revealed by photocurrent nanoscopy, Nat. Nanotechnol. **12**, 31 (2016).

[7] P. Klarskov, H. Kim, V. L. Colvin, and D. M. Mittleman, Nanoscale laser terahertz emission microscopy, ACS Photonics **4**, 2676 (2017).

[8] J. Ma, R. Shrestha, J. Adelberg, C.-Y. Yeh, Z. Hossain, E. Knightly, J. M. Jornet, and D. M. Mittleman, Security and eavesdropping in terahertz wireless links, Nature **563**, 89 (2018).

[9] A. Rice, Y. Jin, X. F. Ma, X. C. Zhang, D. Bliss, J. Larkin, and M. Alexander, Terahertz optical rectification from ⟨110⟩ zinc-blende crystals, Appl. Phys. Lett. **64**, 1324 (1994).

[10] G. Gallot and D. Grischkowsky, Electro-optic detection of terahertz radiation, J. Opt. Soc. Am. B **16**, 1204 (1999).

[11] J. Savolainen, S. Ahmed, and P. Hamm, Two-dimensional Raman-terahertz spectroscopy of water, Proc. Natl. Acad. Sci. **110**, 20402 (2013).

[12] C. Riek, D. V. Seletskiy, A. S. Moskalenko, J. F. Schmidt, P. Krauspe, S. Eckart, S. Eggert, G. Burkard, and A. Leitenstorfer, Direct sampling of electric-field vacuum fluctuations, Science **350**, 420 (2015).

[13] I. C. Benea-Chelmus, F. F. Settembrini, G. Scalari, and J. Faist, Electric field correlation measurements on the electromagnetic vacuum state, Nature **568**, 202 (2019).

[14] J. van Tilborg, D. J. Bakker, N. H. Matlis, and W. P. Leemans, Spectral sidebands on a narrow-bandwidth optical probe as a broad-bandwidth THz pulse diagnostic, Opt. Express **19**, 26634 (2011).

[15] N. van der Valk, P. Planken, A. Buijserd, and H. Bakker, Influence of pump wavelength and crystal length on the phase matching of optical rectification, J. Opt. Soc. Am. B **22**, 1714 (2005).

[16] T. Kampfrath, J. Nötzold, and M. Wolf, Sampling of broadband terahertz pulses with thick electro-optic crystals, Appl. Phys. Lett. **90**, 231113 (2007).

[17] C. Kübler, R. Huber, S. Tübel, and A. Leitenstorfer, Ultrabroadband detection of multi-terahertz field transients with GaSe electro-optic sensors: Approaching the near infrared, Appl. Phys. Lett. **85**, 3360 (2004).

[18] B. Bartal, J. Hebling, K.-L. Yeh, K. A. Nelson, and M. C. Hoffmann, Generation of high-power terahertz pulses by tilted-pulse-front excitation and their application possibilities, J. Opt. Soc. Am. B **25**, B6 (2008).

[19] H. Hirori, A. Doi, F. Blanchard, and K. Tanaka, Single-cycle terahertz pulses with amplitudes exceeding 1 MV/cm generated by optical rectification in $LiNbO_3$, Appl. Phys. Lett. **98**, 091106 (2011).

[20] F. Blanchard, B. E. Schmidt, X. Ropagnol, N. Thiré, T. Ozaki, R. Morandotti, D. G. Cooke, and F. Légaré, Terahertz pulse generation from bulk GaAs by a tilted-pulse-front excitation at 1.8 μm, Appl. Phys. Lett. **105**, 241106 (2014).

[21] M. I. Bakunov and S. B. Bodrov, Terahertz generation with tilted-front laser pulses in a contact-grating scheme, J. Opt. Soc. Am. B **31**, 2549 (2014).

[22] Z. Ollmann, J. A. Fülöp, J. Hebling, and G. Almási, Design of a high-energy terahertz pulse source based on ZnTe contact grating, Opt. Commun. **315**, 159 (2014).

[23] M. Tsubouchi, K. Nagashima, F. Yoshida, Y. Ochi, and M. Maruyama, Contact grating device with Fabry-Perot resonator for effective terahertz light generation, Opt. Lett. **39**, 5439 (2014).

[24] F. Yoshida, K. Nagashima, M. Tsubouchi, M. Maruyama, and Y. Ochi, THz pulse generation using a contact grating device composed of TiO_2/SiO_2 thin films on $LiNbO_3$ crystal, J. Appl. Phys. **120**, 183103 (2016).

[25] M. Tani, K. Horita, T. Kinoshita, C. T. Que, E. Estacio, K. Yamamoto, and M. I. Bakunov, Efficient electro-optic sampling detection of terahertz radiation via Cherenkov phase matching, Opt. Express **19**, 19901 (2011).

[26] W. Cui, A. W. Schiff-Kearn, E. Zhang, N. Couture, F. Tani, D. Novoa, P. St. J. Russell, and J. M. Ménard, Broadband and tunable time-resolved THz system using argon-filled hollow-core photonic crystal fiber, APL Photonics **3**, 111301 (2018).

[27] A. Halpin, N. Couture, and J. M. Ménard, Optical pulse structuring in gas-filled hollow-core kagomé PCF for generation and detection of phase-locked multi-THz pulses [Invited], Opt. Mater. Express **9**, 3115 (2019).

[28] H. Kogelnik, Coupled wave theory for thick hologram gratings, Bell Syst. Tech. J. **48**, 2909 (1969).

[29] T. D. Dorney, R. G. Baraniuk, and D. M. Mittleman, Material parameter estimation with terahertz time-domain spectroscopy, J. Opt. Soc. Am. A **18**, 1562 (2001).

[30] W. L. Bond, Measurement of the refractive indices of several crystals, J. Appl. Phys. **36**, 1674 (1965).

[31] D. F. Parsons and P. D. Coleman, Far infrared optical constants of gallium phosphide, Appl. Opt. **10**, 1683 (1971).

[32] S. Casalbuoni, H. Schlarb, B. Schmidt, P. Schmüser, B. Steffen, and A. Winter, Numerical studies on the electro-optic detection of femtosecond electron bunches, Phys. Rev. Special Top.—Accelerators Beams **11**, 072802 (2008).

[33] A. Leitenstorfer, S. Hunsche, J. Shah, M. C. Nuss, and W. H. Knox, Detectors and sources for ultrabroadband electro-optic sampling: Experiment and theory, Appl. Phys. Lett. **74**, 1516 (1999).

[34] M. Porer, J. M. Ménard, and R. Huber, Shot noise reduced terahertz detection via spectrally postfiltered electro-optic sampling, Opt. Lett. **39**, 2435 (2014).

[35] S. Ahmed, J. Savolainen, and P. Hamm, Detectivity enhancement in THz electrooptical sampling, Rev. Sci. Instrum. **85**, 013114 (2014).

Correction: Equations (1) and (2) contained typographical errors and have been fixed.